Efficiently enhanced N_2 photofixation performance of sea-urchin-like $W_{18}O_{49}$ microspheres with Mn-doping

Zihao Ying, Shengtao Chen, Shuai Zhang, Tianyou Peng*, Renjie Li*

College of Chemistry and Molecular Sciences, Wuhan University, Wuhan 430072, PR China

ABSTRACT

The urgency of mitigating climate change has prompted us to seek more sustainable approach to ammonia (NH_3) synthesis *via* dinitrogen (N_2) photofixation process by using clean solar energy. Herein, a series of Mn-doped sea-urchin-like monoclinic $W_{18}O_{49}$ microspheres (Mn-$W_{18}O_{49}$), which are constructed by nanorods with [010] growth orientation, are fabricated using a facile solvothermal process. It is found that the Mn^{2+} ions can replace the W sites in the $W_{18}O_{49}$ lattice and intervene the formation of microsphere-like structure, but facilitate the photoinduced charge separation and migration in Mn-$W_{18}O_{49}$, and thus cause a promoted N_2 photofixation ability compared with the single $W_{18}O_{49}$. Moreover, the surface Mn^{2+} sites in the monoclinic nanorods of $W_{18}O_{49}$ microspheres paly multiple roles in promoting the chemisorption of N_2 and H_2O molecules and weakening the ultra-stable N≡N bond for the NH_3 production through proton coupling process. Among those Mn-$W_{18}O_{49}$ products fabricated, 3.0% Mn-doped $W_{18}O_{49}$ product achieves the highest NH_3 production activity of 97.9 μmol g^{-1} h^{-1} under Xe-lamp's full spectrum irradiation, 2.3 times higher than that of the single $W_{18}O_{49}$. The present sea-urchin-like Mn-$W_{18}O_{49}$ exhibits both excellent durability and efficient N_2 photofixation ability, which are of significance in sunlight utilization for artificial N_2 fixation and renewable energy conversion.

1. Introduction

Ammonia (NH_3) synthesis has been thought as the cornerstone of modern agriculture and chemical industry for the past centuries, and the Haber-Bosch process is the most economical route for NH_3 synthesis through dinitrogen (N_2) fixation in the world [1,2]. However, almost ~2% of the world's annual energy supply was used in this single reaction only for maintaining the necessary high temperature (~300 °C) and high pressure (over 100 atm) condition, and the major resource of H_2 in the N_2 fixation process originates from industrial steam-reforming of natural gas, which would also generate large quantities of CO_2 [3]. Therefore, it is significantly meaningful to explore an artificial N_2 fixation reaction only use water as H resource under mild condition. In 1977, Schrauzer and Guth firstly reported that TiO_2-based materials have an ability to reduce N_2 into NH_3 under UV light irradiation [4]. After that, lots of semiconducting materials such as metal oxides/sulfides [5–7], bismuth oxyhalides [8–10], and carbonaceous matters [11] have been explored in this area.

Over the past years, tungsten suboxides (WO_{3-x}) have been intensively investigated because of the distinctive physical and chemical properties. Among them, $W_{18}O_{49}$ is one of the most investigated ones because of its stable defect structure and promising properties [12]. In

1986, WO_{3-x} was firstly used as photocatalysts for N_2 reduction, it confirmed that the $WO_{2.96}$ is active species and the N_2 was reduced to NH_3 through a thermal chemical reaction (but not a photochemical one) [13]. More recently, Mo-doped $W_{18}O_{49}$ ultrathin nanowires were fabricated and delivered a N_2 photofixaiton ability under a mild reaction condition, and it was found that the doped Mo species act as active sites for enhancing the chemisorption of N_2 molecules [14]. Also, it was reported that g-C_3N_4/$W_{18}O_{49}$ and Ag/g-C_3N_4/$W_{18}O_{49}$ heterojunctions have full-spectrum-driven N_2 photofixation ability. Among which, $W_{18}O_{49}$ mainly plays a role as light absorber to form more photogenerated electrons for recombining the holes in the g-C_3N_4 through "Z-scheme" mechanism, and Ag loading can promote the electron-hole pair separation [15,16].

Since most of researches are based on the simulation of biological N_2 fixation of the nitrogenase [17–20], the doping elements of N_2 fixation materials are mainly focused on Fe and/or Mo [21–25]. Although some researchers discovered that the Mo ions doped in semiconductor could enhance the N_2 chemisorption and activation abilities [14,26], most of them are not efficient visible-light-driven photocatalysts, which lead to low sunlight utilization and catalytic efficiency during the N_2 photofixation process. Therefore, developing new doped photocatalysts with more efficient, resourceful, wide spectral response

* Corresponding authors.
  E-mail addresses: typeng@whu.edu.cn (T. Peng), lirj@whu.edu.cn (R. Li).

and stable performance is full of significance for N_2 photofixation reaction. From this perspective, Mn, as a more resourceful element in the earth, would be attractive doping element even though there is no investigation on Mn-doped semiconductors for photocatalytic N_2 photofixaion application as far as we know.

Herein, a series of Mn-doped sea-urchin-like monoclinic $W_{18}O_{49}$ microspheres (Mn-$W_{18}O_{49}$), which are constructed by nanorods with [010] growth orientation and diameter of 5–10 nm, were synthesized *via* a facile solvothermal process. It was found that Mn^{2+} ions can replace the W sites of monoclinic $W_{18}O_{49}$ nanorods and intervene the formation of microsphere-like morphology of $W_{18}O_{49}$, but it does not change the growth orientation and shape of the nanorods in Mn-$W_{18}O_{49}$. Moreover, it is firstly found that Mn^{2+}-doped sites in $W_{18}O_{49}$ can not only act as chemisorption and activation centers of N_2 and H_2O molecules, but also facilitate the photoinduced charge separation and migration in Mn-$W_{18}O_{49}$, and thus cause an efficiently enhanced N_2 photofixaiton ability compared to the single $W_{18}O_{49}$ microspheres under full spectrum (UV–vis) or visible light irradiation of Xe-lamp. The effects of Mn doping on the microstructure, optical absorption, photoinduced charge separation and photocatalytic N_2 fixation ability of the Mn-$W_{18}O_{49}$ are discussed detailed.

2. Experimental

2.1. Material syntheses

Mn-doped $W_{18}O_{49}$ microspheres were prepared *via* a facile solvothermal process. Typically, 1.0 mmol WCl_6 was dissolved in 35 mL of ethanol, which was vigorously stirred to obtain a yellow transparent solution, then different amount of $MnCl_2 \cdot 4H_2O$ was added into the solution. After further stirring for 5 min, the resultant solution was put into a Teflon-lined stainless autoclave (volume of 40 mL) and treated at 180 °C for 24 h. After cooled to the room temperature, the deep blue precipitate was separated and washed with deionized water and ethanol for three times, and then dried in the vacuum oven at 70 °C for 10 h to obtain Mn-doped $W_{18}O_{49}$ microspheres.

By varying the addition amount of Mn species, Mn-doped $W_{18}O_{49}$ microspheres containing different Mn-doping contents were produced and denoted as xMn-$W_{18}O_{49}$ products, where x is the molar percentage of the doped Mn species. Also, the single $W_{18}O_{49}$ was synthesized through the same reaction condition without the addition of Mn resource. The Mn and W elemental composition in those xMn-$W_{18}O_{49}$ products are determined using ICP-AES technique. As seen in Table 1, the actual Mn-doping content is basically close to the respective addition contents during the synthesis process.

2.2. Materials characterization

The crystal phases of samples were analyzed based on the X-ray diffraction (XRD) patterns detected using a Bruker D8 advance X-ray diffractometer with Cu Kα irradiation (λ = 0.154178 nm) operated at 40 kV and 40 mA with a scan rate of 5° min^{-1} in the range of 2θ = 20°-70° and 1° min^{-1} in the rage of 2θ = 20°-35° with the commercial pure $SrTiO_3$ as reference matter. The morphologies and microstructures were characterized using Zeiss-Sigma field emission scanning electron microscope (FESEM) and JEOL LaB$_6$ JEM-2100 (HR) high-resolution transmission electron microscope (HRTEM). X-ray photoelectron

spectra (XPS) were conducted on a VG Multilab 2000 spectrometer (Thermo Elctron) with Al Kα source. The absorption spectra were performed using diffuse reflection spectra (DRS, Shimadazu UV-3600), and photoluminescence (PL) spectra were carried out on a Hitachi Model F-6800 fluorescence spectrophotometer. The concentrations of manganese and tungsten were determined by the ICP-AES method using a Thermo Fisher IRIS Intrepid II XSP. Liquid N_2 adsorption-desorption isotherms at 77 K were performed by a Micrometrics ASAP 2460 system. N_2 temperature-programmed-desorption-mass spectrum (N_2-TPD-MS) were determined by using Autochem II (TPD)-Cirrus 2 (MS). The sample was firstly heated to 300 °C in flowing Ar for 3 h, and purge high pure N_2 for 1 h under the room temperature, and then Ar purge the sample for 1 h to decrease the physical adsorbed N_2 on the surface. Finally, the sample heated to 850 °C at a heating rate of 10 °C min^{-1} under Ar flowing. Electron paramagnetic resonance (EPR) spectra were collected on a MS-5000 spectrometer at room temperature.

Transient photocurrent curve was obtained by using a CHI model 618C electrochemical analyzer and a standard three-electrode system, in which platinum electrode, silver-chlorine silver electrode and sample electrode acted as the counter electrode, reference electrode and work electrode, respectively. As for the preparation of work electrode, 1.0 mg of sample was dispersed into 0.5 mL of Nafion ethanol solution (0.05 wt %) under stirring and sonication for 3 min, then the result solution was dripped on clean fluorine-doped tin oxide (FTO) glass. The film with 1.0 cm^2 active area was readied for photocurrent and after air-drying for at least 30 min. In general, the three electrodes were immersed into a Na_2SO_4 solution (0.5 M) and well connected with the analyzer. Before irradiation, the suspension was continuously purged by N_2 to remove O_2, and then illuminated by visible light ($\lambda > 400$ nm) of 300 W Xe-lamp with an additional cutoff filter.

The measurement of flat-band potential (E_{fb}) were almost same as the test of transient photocurrent curve, the reference electrode was still silver-chlorine silver electrode (0.5 M Na_2SO_4 solution, E^θ = 0.198 V *vs.* NHE), and the E_{fb} value was determined by the Mott-Schottky relation [27]:

$$C^{-2} = (2/e\varepsilon\varepsilon_0 N_d)[V_a - E_{fb} - kT/e]$$

where, C is space charge layer capacitance, e is electron charge, ε is dielectric constant, ε_0 is permittivity of vacuum, N_d is electron donor density, V_a is the applied potential, and E_{fb} is flat band potential.

2.3. Photocatalytic activity measurement

The N_2 photofixation activity was measured using a home-made vessel illuminated by the full spectrum of a 300 W Xe-lamp or the visible light ($\lambda > 400$ nm) from the same Xe-lamp with an additional cutoff filter. The typical full spectrum of the Xe-lamp mainly locates in UV–vis range with wavelengths of 320–780 nm (Fig. S1) since the NIR irradiation of Xe-lamp was filtered with a reflector mirror. Generally, 15 mg of photocatalyst was dispersed into 150 mL of Na_2SO_3 solution (1.0 mM) as hole sacrificial agent. Before the irradiation, N_2 flow was bubbled into the suspension for 20 min to remove the dissolved O_2. The N_2 flow could be imported into an Erlenmeyer flask with H_2SO_4 solution to absorbed the tail gas. During the photocatalytic experiment, the vessel was cooled to room temperature with a flow of cooling water and the experiment continued 2 h. The NH_3 production amount was spectrophotomertrically determined using indophenol blue method, and the

Table 1
Elemental composition ratios of the obtained xMn-$W_{18}O_{49}$ products detected by ICP-AES technique.

x value	0	1%	3%	5%	7%	15%
W / mg g^{-1}	659.6 ± 4.6	648.2 ± 3.9	625.8 ± 6.0	675.6 ± 3.6	632.4 ± 2.6	648.4 ± 1.7
Mn / mg g^{-1}	0	0.9 ± 0.03	4.0 ± 0.1	8.8 ± 0.3	12.4 ± 0.1	28.1 ± 0.1
Mn molar percentage / %	0	0.5	2.14	4.36	6.56	14.50

average NH$_3$ production activity was calculated from the results of at least three parallel experiments. In addition, all photocatalysts have conducted blank test using Ar replacing N$_2$, which confirmed all color development reaction was stemmed from the N$_2$ photofixation process but not the false appearance by the photocatalyst itself.

For the measurement of recycling stability, five consecutive NH$_3$ production runs for total 20 h irradiation was performed under the same conditions. After one cycle for 4 h light irradiation, the photocatalyst was recovered by centrifugation and dried in vacuum oven, and then added in a new solution of sacrificial agent for the next run. Monochromatic light used in the measurement of apparent quantum efficiency (AQE) was acquired by inserting an appropriate band-pass filter ahead of the 300 W Xe-lamp to obtain the correct monochromatic light, and the value of light intensity was measured by using a SRC-1000-TC-QZ-N monocrystalline silicon cell (Oriel, USA). Each light intensity was calculated by the average intensity of nine point in the light spot which was chose uniformly at cross line. The NH$_3$ yields were measured after 2 h photoreaction, and the AQE was calculated on the basis of the following equation [10]:

$$AQE\% = \frac{6\times \text{ number of evolved ammonia molecules}}{\text{number of incident photons}} \times 100\%$$

3. Results and discussion

3.1. Crystal phase and valence state analyses

The X-ray diffraction (XRD) patterns of all Mn-doped products are very similar to that of the single one without Mn-doping (Fig. 1a), which delivers obvious diffraction peaks at $2\theta = 23.3°$ and $47.7°$ ascribable to the reflections of (010) and (020) planes of monoclinic W$_{18}$O$_{49}$ (JCPDS No. 71-2450) [28], respectively. By using a commercial SrTiO$_3$ as reference to mix with those Mn-doped W$_{18}$O$_{49}$ products (xMn-W$_{18}$O$_{49}$), a gradual shift in the (010) peak of monoclinic W$_{18}$O$_{49}$ along with the increase of Mn-doping level can be confirmed (Fig. 1b), while no shift is observed from the (100) (at $2\theta = 22.6°$) and (110) (at $2\theta = 32.3°$) peaks of cubic SrTiO$_3$ (JCPDS No. 73-0661) [29]. This shift of (010) peak (up to 0.22° for 15% Mn-W$_{18}$O$_{49}$) toward higher 2θ angle implies that Mn species might dope into the crystal lattice of monoclinic W$_{18}$O$_{49}$.

The survey X-ray photoelectron spectra (XPS, Fig. 2a) indicate that those xMn-W$_{18}$O$_{49}$ products have obvious binding energy (BE) peaks of W4f and O1s in addition to weak one of Mn2p at ~640 eV [30,31]. Along with the increase of Mn-doping level, the high resolution Mn2p spectra (Fig. 2b) present increasingly enhanced BE peaks at 641.8 eV (Mn^{2+} 2p$_{3/2}$) and 653.9 eV (Mn^{2+} 2p$_{1/2}$) of Mn^{2+}, and the satellite feature located in the range of 645–650 eV further confirms the Mn species is divalent (but not quadrivalent) [31–33]. The high resolution W4f spectrum (Fig. 2c) of the single W$_{18}$O$_{49}$ can be de-convoluted into

two main BE peaks at 36.1 eV (W^{6+} 4f$_{7/2}$) and 38.2 (W^{6+} 4f$_{5/2}$) eV in addition to weak doublets at 34.7 and 36.9 eV, which can be assigned to the emission of W^{5+} 4f$_{7/2}$ and W^{5+} 4f$_{5/2}$ core level from W^{5+} [34–36]. It suggests the coexistence of W^{6+}/W^{5+} ions in the W$_{18}$O$_{49}$ lattice. Moreover, the BE peak positons for those xMn-W$_{18}$O$_{49}$ products ($0 < x \leq 7\%$) shift $ca.$ 0.26 eV toward lower BE values, implying that Mn^{2+} doping can influence the chemical environments of W^{6+}/W^{5+} ions in the W$_{18}$O$_{49}$ lattice. As shown in Fig. 2d, the O1s spectrum of the single W$_{18}$O$_{49}$ can be deconvoluted into two symmetrical peaks at 530.9 and 531.9 eV, ascribable to the crystal lattice oxygen bonded with W atoms (W−O−W) and the surface oxygen of −OH species (W−OH) [37–39]. Similarly, the BE peaks at ~530.7 and ~531.8 eV for those xMn-W$_{18}$O$_{49}$ products also can be ascribed to the crystal lattice oxygen and the surface −OH group, respectively. In addition, a weak peak at 530.0 eV, ascribable to the oxygen atoms of Mn-O species, can be observed from those xMn-W$_{18}$O$_{49}$ products with x higher than 3% [32,33].

The above results demonstrate that the Mn^{2+} ions are doped into the W$_{18}$O$_{49}$ lattice, and it can be conjectured that substitutional solid solution is formed in those xMn-W$_{18}$O$_{49}$ products according to the Hume-Rothery rule because the ionic radii of W^{6+}/W^{5+} (60/62 pm) in an octahedral coordination are close to that of Mn^{2+} (67 pm), and the electronegativity of W (1.7 Pau) is just slightly larger than that of Mn (1.5 Pau) [40,41]. The peak area ratio of surface −OH group and crystal lattice oxygen in O1s XPS spectra (Fig. 2d) increases from 0.41 ($x = 0$), to 0.45 ($x = 3\%$) and 0.49 ($x = 7\%$), suggesting that more surface defects might be caused by Mn^{2+} replacing the W^{6+}/W^{5+} sites of W$_{18}$O$_{49}$. In addition, the electron paramagnetic resonance (EPR) spectra (Fig. S2) indicate that the single W$_{18}$O$_{49}$ has no any paramagnetic response signal in the range of 300–400 mT, implying there is no obvious oxygen vacancies (V_O) (g = 2.001) existed in the single W$_{18}$O$_{49}$ [9].

Usually, the stoichiometric WO$_3$ lattice consists of WO$_6$ octahedrons with corner connecting, while the structure of nonstoichiometric W$_{18}$O$_{49}$ is distorted and restructured by sharing edges, which intrinsically forms low-valence W species and W − W metallic interaction in the lattice [14], and thus there is no obvious V_O signal. However, a six-line spectrum characteristic of isolated paramagnetic Mn^{2+}, arising from the hyperfine interaction with the ^{55}Mn nuclear spin (I$_{5/2}$) [42], is observed for all xMn-W$_{18}$O$_{49}$ products. Since Mn^{2+} ions instead of W^{6+}/W^{5+} sites in the W$_{18}$O$_{49}$ lattice might lead to the formation of V_O sites for maintaining the charge balance in Mn-W$_{18}$O$_{49}$, which would show an EPR signal at g = 2.001 [9]. Nevertheless, the increase of Mn^{2+}-doping level causes a gradually enhanced EPR signals of Mn-W$_{18}$O$_{49}$, but there is no any obvious EPR signal at g = 2.001 for free electrons in V_O sites (Fig. S2), suggesting that electrons might prefer to be captured by Mn^{2+} ions rather than delocalized over the W$_{18}$O$_{49}$ lattice [14], which would be a benefit to the photocatalytic process of N$_2$ fixation. Furthermore, the increasing trends of EPR signal intensity (Fig. S2) and peak area ratios in O1s XPS spectrum (Fig. 2d)
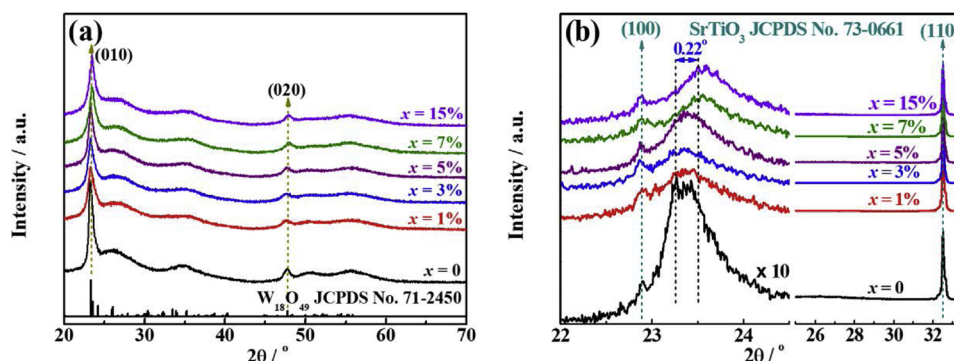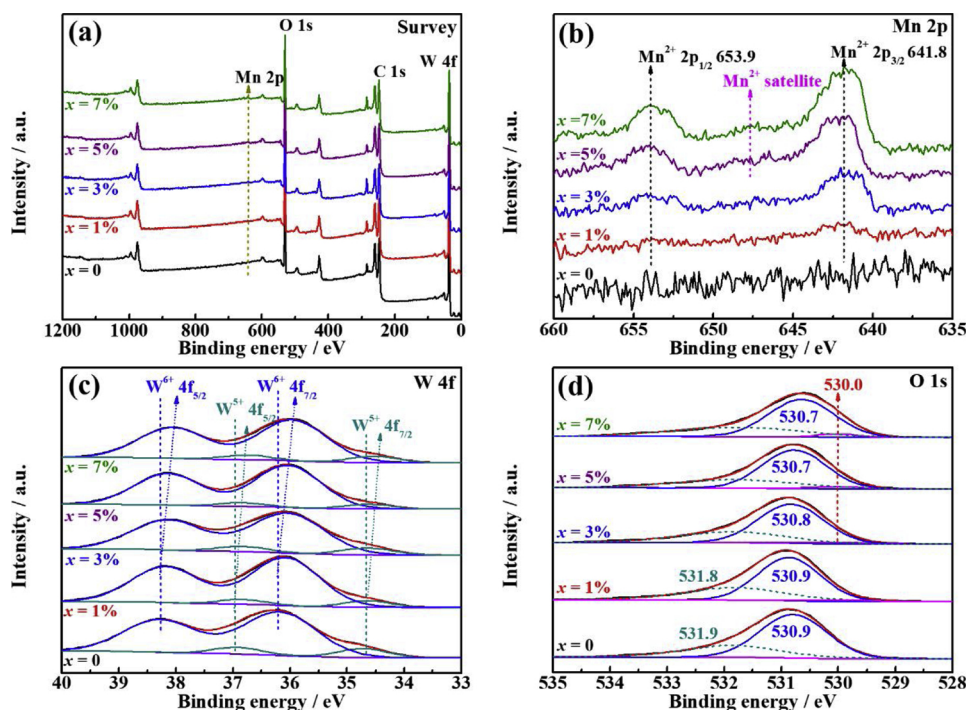

Fig. 1. (a) XRD patterns of the obtained xMn-W$_{18}$O$_{49}$ ($x = 0$–15%) products derived from different Mn-doping levels. (b) XRD patterns at the lower angle regions ($2\theta = 22°$-25° and 25°-33.5°) of the mixtures containing xMn-W$_{18}$O$_{49}$ and SrTiO$_3$.

Fig. 2. The Survey and high resolution XPS spectra of the obtained xMn-$W_{18}O_{49}$ products with Mn-doping levels at 0–7%. (a) Survey, (b) Mn 2p (b), (c) W 4f and (d) O 1s.

demonstrate that the enhanced surface defects can be mainly ascribed to the surface Mn^{2+} doped sites when the Mn-doping level is enhanced from 0 to 7%, which can also enhance the reaction possibility for N_2 photofixation as will be discussed below.

3.2. Microstructure and morphology analyses

FESEM image depicted in Fig. 3a exhibits that the single $W_{18}O_{49}$ has sea-urchin-like microsphere morphology with sizes in the range of 1–2 μm. Although the sea-urchin-like multilevelled structures can be maintained upon enhancing the Mn-doping levels (Fig. 3b-d), the

microsphere-like morphology is destructed gradually and changed into irregular ones. It implies that the Mn^{2+} doping would intervene the formation of microsphere-like structure. TEM image (Fig. 4a) shows that the sea-urchin-like microsphere is mainly constructed by regular nanorods with diameter in the range of 5–10 nm, and the HRTEM image (Fig. 4b) exhibits that the d-spacings of lattice fringes are $ca.$ 0.377 nm and 0.370 nm, similar to the theoretical values of (010) and (103) facets of monoclinic $W_{18}O_{49}$ [14], respectively. Besides, the Fast Fourier Transform (FFT) pattern displays obvious diffraction spots. These results infer that the single $W_{18}O_{49}$ microsphere has high crystallinity, and its nanorods grow along the [010] orientation of monoclinic
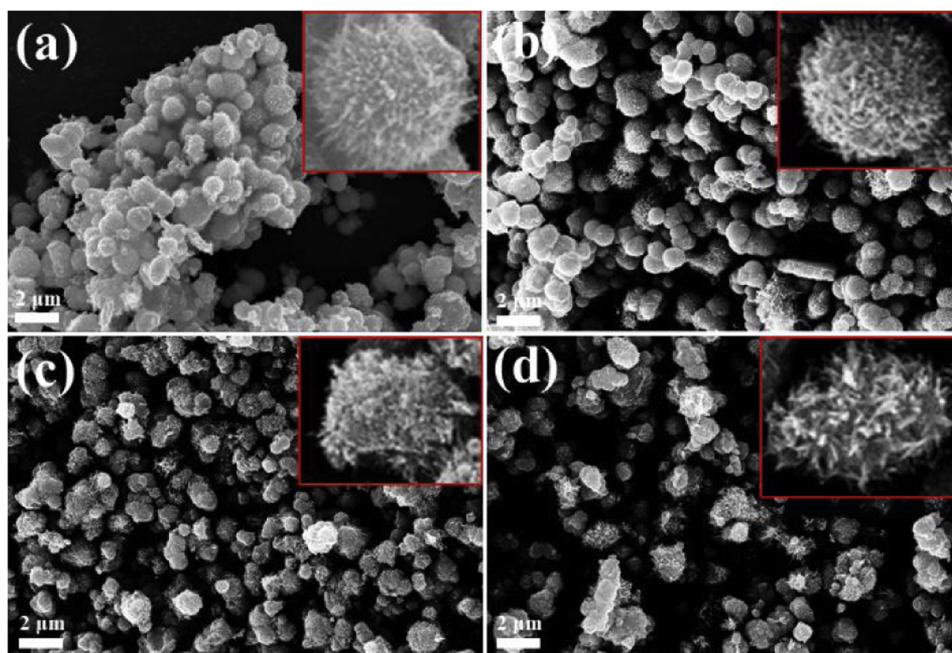
Fig. 3. Typical FESEM images of the obtained xMn-$W_{18}O_{49}$ products with x = 0 (a), 3% (b), 7% (c), 15% (d).
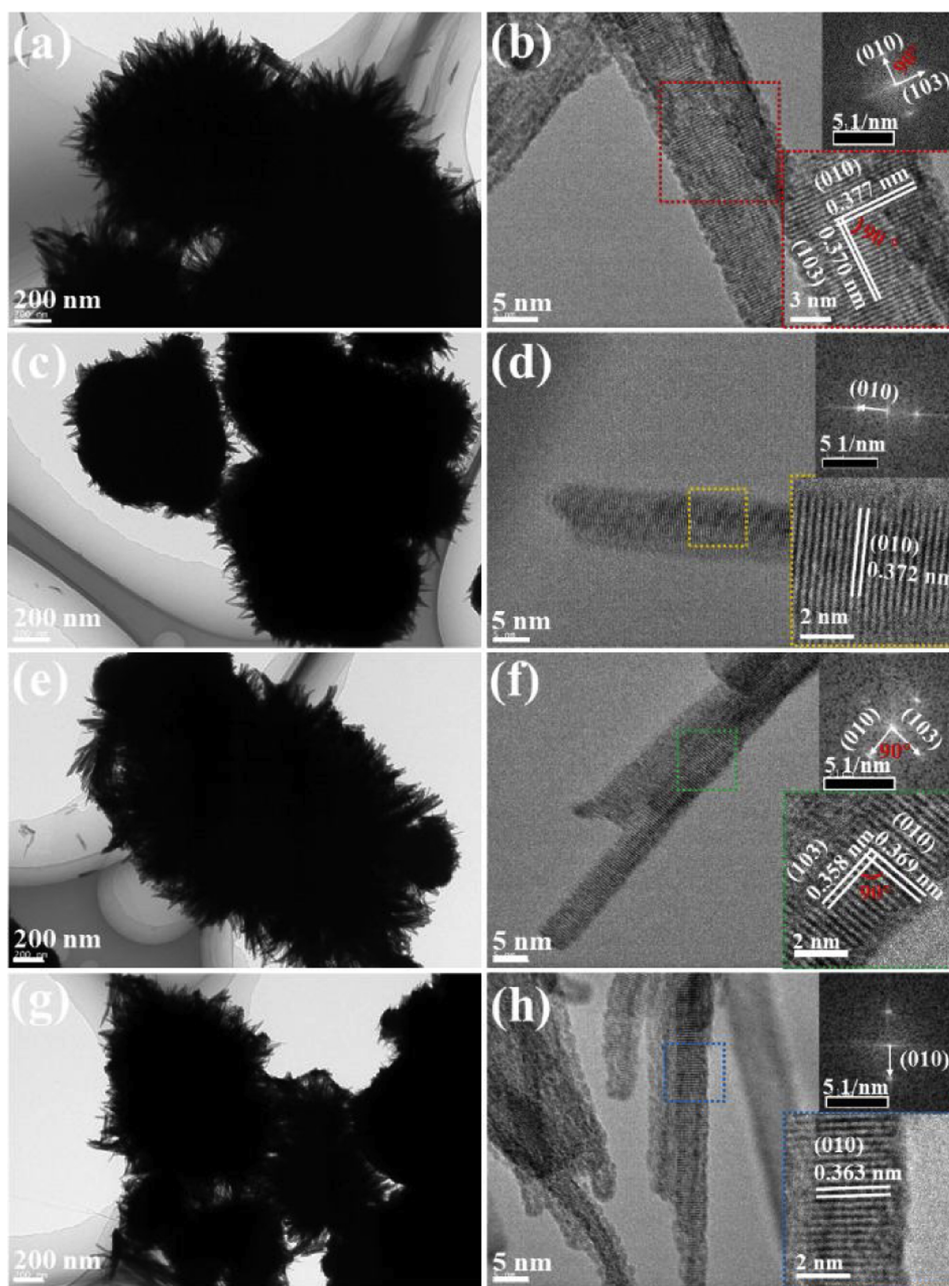
Fig. 4. Typical TEM (a, c, e, g) and HRTEM (b, d, f, h) images of the obtained xMn-$W_{18}O_{49}$ products with x = 0 (b), 3% (d), 7% (f) and 15% (h).

$W_{18}O_{49}$. Similarly, 3% Mn-$W_{18}O_{49}$ still shows sea-urchin-like morphology constructed by nanorods (Fig. 4c), while the HRTEM image indicates that the *d*-spacing of lattice fringes for the nanorod is 0.372 nm (Fig. 4d), which is slightly lower than that of (010) plane of $W_{18}O_{49}$.

Although the microsphere-like morphology become more irregular along with the increase of Mn-doping level to 7% (Fig. 4e) and 15% (Fig. 4g), those nanorod-like structures are still remained. It can be found that the *d*-spacings (*ca.* 0.369 and 0.363 nm) of lattice fringes for 7% Mn-$W_{18}O_{49}$ (Fig. 4f) and 15% Mn-$W_{18}O_{49}$ (Fig. 4h) are lower than that (0.377 nm) of (010) plane for the single $W_{18}O_{49}$, implying that Mn^{2+} doping leads to the decrease in the *d*-spacings of $W_{18}O_{49}$. The above results indicate that Mn^{2+} doping would influence the formation of sea urchin-like microspheres with regular shape, but it does not affect the [010] growth orientation of $W_{18}O_{49}$ nanorods, and therefore Mn-$W_{18}O_{49}$ products still maintain sea-urchin-like multilevel structures constructed by nanorodes.

Liquid N_2 adsorption-desorption isotherms (Fig. S3a) indicate that all xMn-$W_{18}O_{49}$ products exhibit type II isotherms with H3 hysteresis loops, which is similar to that of the single $W_{18}O_{49}$. Along with the increase of Mn-doping level from 0 to 7%, the xMn-$W_{18}O_{49}$ products display a significant decreasing trend (from 162.1 to 103.9 $m^2\,g^{-1}$) in the Brunauer-Emmett-Teller (BET) specific surface area (S_{BET}). On the other hand, the Barret-Joyner-Halenda (BJH) pore size distribution plots (Fig. S3b) derived from the desorption branch reveal that the average pore diameter of xMn-$W_{18}O_{49}$ products exhibits a slight increase (6.6 nm to 8.2 nm) along with the decrease in the small pores with pore size in the range of 3–5 nm upon enhancing the Mn-doping level from 0 to 7%. These changes in micro/mesoporous structures can be due to the differences in the sea-urchin-like multilevelled structure of those xMn-$W_{18}O_{49}$ products caused by the various Mn^{2+} doping levels, which will further influence the photoactivity as mentioned below.

3.3. Photocatalytic activity analyses

To investigate the photoactivities of xMn-$W_{18}O_{49}$ products, the photoreaction conditions for N_2 fixation were optimized under full spectrum irradiation of Xe-lamp, and the quantitative determination of NH_3 produced in the photoreaction suspension and the tail gas absorption solution was performed using chromogenic reaction with indophenol blue method [43]. A blank experiment with Ar flow instead of N_2 demonstrated that no NH_3 was produced from the irradiated photoreaction suspension. Since the raw sources are chlorides such as WCl_6 and $MnCl_2$, those xMn-$W_{18}O_{49}$ products have no N-species remained during the material synthesis processes. This issue can be confirmed by the high resolution N1 s XPS spectra of those xMn-$W_{18}O_{49}$ products (Fig. S4), from which no obvious BE peak of N species can be observed. The above results suggest that the NH_3 production is derived from the N_2 photofixation reaction in the present photoreaction system.

Also, the effect of photocatalyst dosage on the NH_3 production activity of the 3%Mn-$W_{18}O_{49}$ suspension (in 150 mL of 1.0 mM Na_2SO_3 solution) under the full spectrum illumination of Xe-lamp. As seen from Fig. S5, 15 mg of photocatalyst exhibits the best NH_3 production activity, and thus is an optimal photocatalyst dosage in the present photoreaction system. Under this photoreaction conditions, the single $W_{18}O_{49}$ delivers a very limited N_2 photofixation activity $(29.3 \mu mol\,g^{-1}\,h^{-1})$ under Xe-lamp full spectrum illumination (Fig. 5a), while all xMn-$W_{18}O_{49}$ products deliver higher activities for N_2 photoreduction toward NH_3, indicating that the Mn^{2+} doping could efficiently improve the N_2 photofixation performance of $W_{18}O_{49}$. Along with the increase of Mn-doping level, the N_2 photofixation activity of xMn-$W_{18}O_{49}$ products shows a firstly increasing trend and then a decreasing one, and 3% Mn-$W_{18}O_{49}$ achieves the highest N_2 photofixation ability with an average NH_3 production activity of $97.9 \mu mol\,g^{-1}\,h^{-1}$ under the full spectrum illumination, which is 2.3 times higher than that of the single $W_{18}O_{49}$. Similarly, the N_2 photofixation activity of xMn-$W_{18}O_{49}$ products shows a firstly increasing trend and then a decreasing one under visible light ($\lambda > 400$ nm) irradiation, and 3% Mn-$W_{18}O_{49}$ still delivers the highest activity of $33.5 \mu mol\,g^{-1}\,h^{-1}$, which was 3.6 times than that $(7.3 \mu mol\,g^{-1}\,h^{-1})$ of the single $W_{18}O_{49}$.

The above results demonstrate that the optimal Mn-doping level in xMn-$W_{18}O_{49}$ is 3%, thus wavelength-dependent apparent quantum efficiencies (AQE) of 3% Mn-$W_{18}O_{49}$ were determined by detected the produced amount of NH_3 under various monochromatic light irradiations. It was found that the AQE value's changing trend along with the illuminated wavelength matches with the intrinsic absorption capacity of $W_{18}O_{49}$ with wavelength below 435 nm. Specifically, the AQE values at 350 and 435 nm are determined to be 0.14% and 0.023% (Fig. S6), respectively. In addition, 3% Mn-$W_{18}O_{49}$ has relatively stable N_2 photofixation activity during the total 20 h photoreaction for 5 successive recycles (Fig. 5b). The recovered photocatalyst after the photoreaction shows a XRD pattern very similar to that of the original one (Fig. S7), in which the XRD peak positons and intensities of (010) and (020) are

basically identical even after the 3 recycles for photoreaction. Besides, the survey and W4f, O1 s, Mn2p high-resolution XPS spectra (Fig. S8a-d) of 3% Mn-$W_{18}O_{49}$ before and after the photoreaction show no obvious change. These results confirm the reusability and stability of the present Mn-$W_{18}O_{49}$. It should be noticed that the BE peak intensity (at 401.7 eV) of N1 s XPS spectra (Fig. S8e) increases obviously, which is originated from the remnant NH_4^+ after the photoreaction [44]. In addition, the pH value of the photoreaction suspension slightly decreases from 7.37 to 6.28 with prolonging the reaction time from 0 to 4 h (Fig. S9), this slightly decreased pH value also implied that some generated NH_4^+ and SO_4^{2-} dissolved into the photoreaction suspension. Therefore, it can be convinced that the detected NH_3 in the present photoreaction system is stemmed from the N_2 photofixation reaction.

3.4. Photoelectrochemical and surface property analyses

To explore the effects of Mn doping on the N_2 photofixation ability of xMn-$W_{18}O_{49}$ products, photoluminescence (PL) spectra and photocurrent response curves are tested and showed in Fig. 6. As can be seen from Fig. 6a, the PL peak intensity shows a firstly decreasing trend and then an increasing one along with the increase of Mn-doping level from 0 to 7%, and the 3% Mn-$W_{18}O_{49}$ displays the minimum PL peak intensity. It is consistent with the above photocatalytic performance shown in Fig. 5a, and demonstrating that 3% Mn-$W_{18}O_{49}$ has the most efficient charge separation among those xMn-$W_{18}O_{49}$ products [14]. Once the Mn-doping level is higher than 3%, the redundant doping Mn^{2+} ions might act as charge recombination centers of the photogenerated charge, and thus causes the PL peak intensity increase gradually. The photocurrent test results also present a similar conclusion. Among those products, the single $W_{18}O_{49}$ shows the lowest photocurrent response (Fig. 6b), suggesting the single $W_{18}O_{49}$ has the lowest defect concentration and the highest charge combination efficiency. With enhancing the Mn^{2+}-doping level, the photocurrent response values show an increasing trend firstly followed by a rapidly decreasing one, and 3% Mn-$W_{18}O_{49}$ delivers the largest photocurrent value among those products. The high photocurrent value is associated with the facilitated charge separation and migration [45], which might be the main reason that Mn^{2+} doping can improve the N_2 photofixation efficiency.

The chemisorption and activation processes of N_2 molecules are the essential problem in N_2 fixation reactions because of the ultra-stable $N\equiv N$ bond. To further explore this issue, the N_2 temperature programmed desorption-mass spectrum (N_2-TPD-MS) experiments are conducted. In Fig. 7a, the N_2-TPD results indicate that the single $W_{18}O_{49}$ has two desorbed peaks centered at *ca.* 130 and 400 °C, while 3% Mn-$W_{18}O_{49}$ displays three peaks centered at *ca.* 170, 393 and 535 °C. Obviously, the first peak position shifts to a higher temperature and a new weak peak is generated at *ca.* 535 °C. It implies that Mn-doping can change the adsorption property of $W_{18}O_{49}$. With the mass
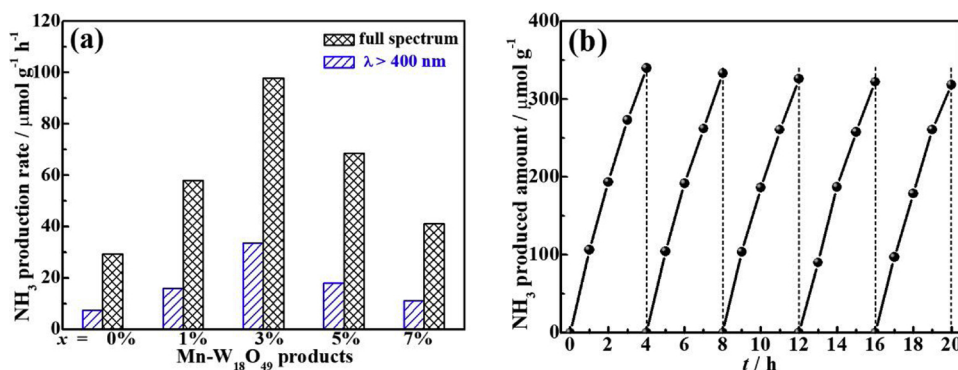
Fig. 5. (a) The average NH_3 production activity of the obtained xMn-$W_{18}O_{49}$ products under full spectrum or visible light ($\lambda > 400$ nm) illumination for 2 h; (b) Cycling photocatalytic behavior towards NH_3 production over 3% Mn-$W_{18}O_{49}$ under full spectrum illumination. Conditions: photocatalyst (15 mg) in Na_2SO_3 (1.0 mM) solution (150 mL), 300 W Xe-lamp.
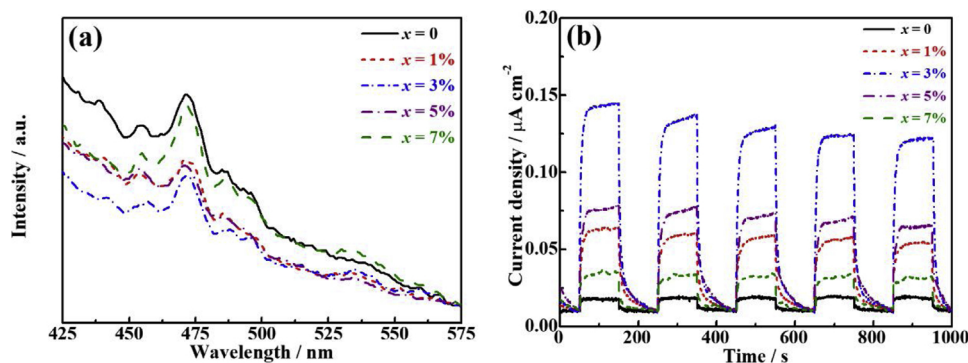
Fig. 6. (a) Photoluminescence (PL) spectra of the obtained xMn-$W_{18}O_{49}$ products with excitation wavelength of 325 nm. (b) photocurrent-time curves of the obtained xMn-$W_{18}O_{49}$ products under visible light ($\lambda > 400$ nm) irradiation.

spectrometer as a detector of the N_2-TPD system, the MS spectra can be detected, and its results are shown in Fig. 7b, in which the MS peaks at 18 and 28 represent the H_2O and N_2 molecules, respectively. As seen, the single $W_{18}O_{49}$ shows two peaks at *ca.* 135 °C and 421 °C in the MS area of H_2O [46], while 3% Mn-$W_{18}O_{49}$ delivers a first peak with the positon shifting toward higher temperature at *ca.* 180 °C. Similarly, 3% Mn-$W_{18}O_{49}$ also delivers a desorbed peak with the positon shifting toward higher temperature at *ca.* 530 °C in the MS area of N_2 compared to the single $W_{18}O_{49}$, which displays an obvious peak centered at *ca.* 470 °C followed a wide peak at *ca.* ~650 °C. Since the desorbed peak shift to higher temperature in TPD analyses represent the promotion of chemisorption ability [46,47], the above peak shifts in the MS areas of H_2O and N_2 molecules imply that the H_2O and N_2 chemisorption ability can be promoted by Mn^{2+} ions doped into the $W_{18}O_{49}$ lattice, which then activate the H–O and N≡N bonds to be more accessible and easier to participate in the photoreaction for N_2 photofixation to NH_3 production.

3.5. Energy band structure and mechanism analyses

To further investigate the photocatalytic performance of the xMn-$W_{18}O_{49}$ products, the energy band structures are investigated. Fig. 8a present the UV–vis diffuse reflectance absorption spectra (DRS). As seen, the single $W_{18}O_{49}$ show an onset absorption edge at *ca.* 513 nm, corresponding to the bandgap energy (E_g) of *ca.* 2.4 eV, which was comparable to the value (~2.6 eV [48]) reported before. With the enhancement of Mn^{2+}-doping level, the products display redshift obviously, and the E_g values of xMn-$W_{18}O_{49}$ decrease along with the increase of the x value. The onset absorption edge of xMn-$W_{18}O_{49}$ with $x = 3\%$ and $x = 7\%$ products were located at 549 nm and 604 nm, which were corresponding to the bandgap energy (E_g) of 2.26 eV and 2.05 eV. The flat-band potentials (E_{fb}) of the single $W_{18}O_{49}$ (Fig. S10a) and 3% Mn-$W_{18}O_{49}$ (Fig. S10b) are determined form those Mott-

Schotty plots. Obviously, both the Mott-Schotty plots show positive slope, implying their n-type semiconducting property. The E_{fb} value of the single $W_{18}O_{49}$ and 3% Mn-$W_{18}O_{49}$ were calculated by the intercepts with x-axis, the values can be determined to 0.36 V and 0.33 V *vs.* NHE [49], respectively. Because of the conduction band (CB) is 0.1 V higher than E_{fb} for n-type semiconductor, the E_{CB} level finally calculated to be 0.26 V and 0.23 V, respectively. The results are comparable to the value (~0.21 eV [48]) reported before. It inferred that the valance band positon (E_{VB}) of the single $W_{18}O_{49}$ and 3% Mn-$W_{18}O_{49}$ can deduced to be 2.52 V and 2.28 V according to the formula of $E_g = E_{VB} - E_{CB}$, respectively. Therefore, the E_{CB} and E_{VB} of the photocatalysts were calculated and a potential energy diagram of xMn-$W_{18}O_{49}$ products can be presented in Fig. 8b. As seen, the E_{CB} levels of both $W_{18}O_{49}$ and 3% Mn-$W_{18}O_{49}$ are more negative than the potential of N_2 converted to NH_4^+ ($N_2 + 8H^+ + 6e^- \rightarrow 2NH_4^+$, $E^0 = 0.27$ V *vs.* NHE [7]), which confirmed that the reaction is accessible from the thermodynamics.

Based on the above experiment results and discussion, a possible N_2 photofixation mechanism over the present Mn-$W_{18}O_{49}$ is proposed in Fig. 8b. Since there is large energy gap (10.82 eV) between the highest occupied molecular orbitals (HOMO) and lowest unoccupied molecular orbitals (LUMO) of N_2 molecules, one or two-electron transfer reaction for N_2 fixation is difficult, whereas a metal center can disrupt the N_2 bonding system, and thus starts N_2 activation toward further reactions, usually by enhancing its LUMO electron density due to more back donation of metal d–p electrons and by decreasing its HOMO electron density upon coordination [1]. As mentioned above, the H_2O and N_2 chemisorption ability can be promoted by the surface Mn^{2+} ions of Mn-$W_{18}O_{49}$, which then activate the H–O and N≡N bonds to be more accessible and easier to participate in the photoreaction for N_2 photofixation to NH_3 production. The sea-urchin-like Mn-$W_{18}O_{49}$ could absorb the UV and visible light and generate photogenerated electrons and holes, and then those photogenerated electrons would transfer to the adsorbed N_2 molecules and form the activated N_2 molecules.
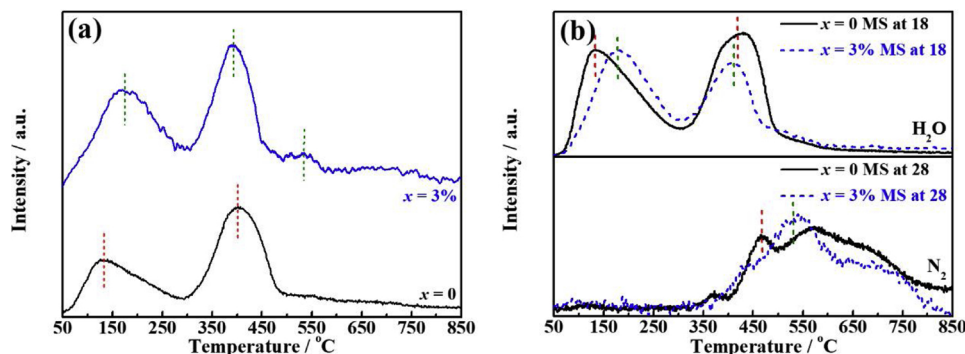
Fig. 7. (a) N_2-TPD results of the xMn-$W_{18}O_{49}$ products ($x = 0$, 3%); (b) N_2-TPD-MS results with MS at 18 and 28 of the xMn-$W_{18}O_{49}$ products ($x = 0$, 3%).
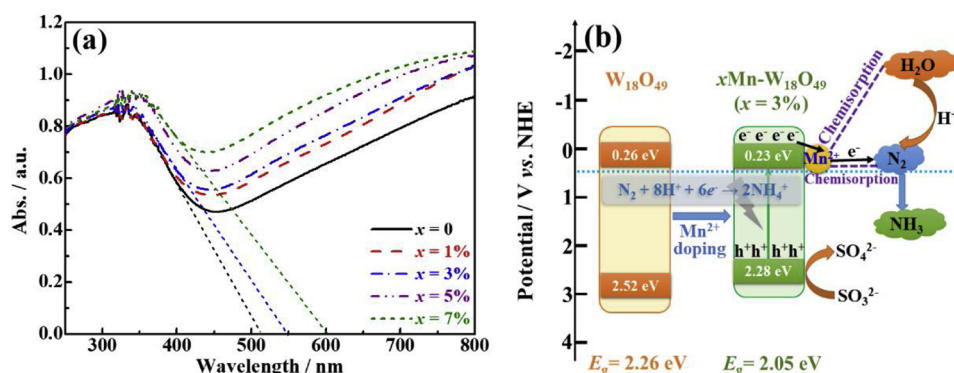
Fig. 8. (a) UV–vis diffuse reflectance absorption spectra (DRS) of the xMn-$W_{18}O_{49}$ products; (b) The possible mechanisms of N_2 photofixation process over Mn-$W_{18}O_{49}$.

Meanwhile, the weaken H–O bonds after chemisorption H_2O molecules would generate more active H^+ ions, which can react with those activated N_2 molecules to produce NH_3 through a proton coupling process. Those photogenerated holes will be consumed by the sacrificial reagent to avoid the recombination of photogenerated carriers. These results presented here are fundamentally important for understanding that Mn^{2+} doping sites could promote the photofixation N_2 efficiency by acting as chemisorption and activation centers of both N_2 and H_2O molecules, and therefore demonstrating a significant advance to more efficiently utilizing the transition metal element for UV/Vis-light-driven photofixation N_2 through doping strategy.

4. Conclusions

In summary, a series of Mn^{2+}-doped sea-urchin-like monoclinic $W_{18}O_{49}$ microspheres (xMn-$W_{18}O_{49}$, $0 \leq x \leq 7\%$), which are constructed by nanorods with [010] growth orientation and diameter of 5–10 nm, were synthesized *via* a facile solvothermal process. Although the Mn^{2+} ions instead of W sites in the monoclinic $W_{18}O_{49}$ nanorods intervene the formation of microsphere-like morphology of $W_{18}O_{49}$, it does not change the growth orientation and shape of the nanorods in Mn-$W_{18}O_{49}$ microspheres. Moreover, it is firstly found that Mn^{2+}-doped sites in $W_{18}O_{49}$ can not only act as chemisorption and activation centers of N_2 and H_2O molecules, but also facilitate the photoinduced charge separation and migration in Mn-$W_{18}O_{49}$, and thus cause an efficiently enhanced N_2 photofixaiton ability toward NH_3 production compared to the single $W_{18}O_{49}$ microspheres under full spectrum or visible light irradiation. The present results provide new insights into the significance of transition metal element doping strategy for efficiently promoting the chemisorption and activation processes of ultrastable N_2 molecules, thus paving new way to the design and synthesis of high-performance, easily available materials for N_2 photofixation under the mild condition.

Acknowledgments

Appendix A. Supplementary data

Supplementary material related to this article can be found, in the online version, at doi:https://doi.org/10.1016/j.apcatb.2019.05.005.

References

[1] H.P. Jia, E.A. Quadrelli, Chem. Soc. Rev. 43 (2014) 547–564.
[2] V. Rosca, M. Duca, M.T. de Groot, M.T.M. Koper, Chem. Rev. 109 (2009) 2209–2244.
[3] S. Licht, B.C. Cui, B.H. Wang, F.F. Li, J. Lau, S.Z. Liu, Science 45 (2015) 637–640.
[4] G.N. Schrauzer, T.D. Guth, J. Am. Chem. Soc. 99 (1977) 7189–7193.
[5] W.R. Zhao, J. Zhang, X. Zhu, M. Zhang, J. Tang, M. Tan, Y. Wang, Appl. Catal. B Environ. 144 (2014) 468–477.
[6] J.H. Yang, Y.Z. Guo, R.B. Jiang, F. Qin, H. Zhang, W.Z. Lu, J.F. Wang, J.C. Yu, J. Am. Chem. Soc. 140 (2018) 8497–8508.
[7] S.M. Sun, X.M. Li, W.Z. Wang, L. Zhang, X. Sun, Appl. Catal. B Environ. 200 (2017) 323–329.
[8] H. Li, J. Shang, J.G. Shi, K. Zhao, L.Z. Zhang, Nanoscale 8 (2016) 1986–1993.
[9] H. Li, J. Shang, Z.H. Ai, L.Z. Zhang, J. Am. Chem. Soc. 137 (2015) 6393–6399.
[10] S.Y. Wang, X. Hai, X. Ding, K. Chang, Y.G. Xiang, X.G. Meng, Z.X. Yang, H. Chen, J.H. Ye, Adv. Mater. 29 (2017) 1701774.
[11] S.Z. Hu, X. Chen, Q. Li, F.Y. Li, Z.P. Fan, H. Wang, Y.J. Wang, B.H. Zheng, G. Wu, Appl. Catal. B Environ. 201 (2017) 58–69.
[12] C.S. Guo, S. Yin, M. Yan, M. Kobayashi, M. Kakihana, T. Sato, Inorg. Chem. 51 (2012) 4763–4771.
[13] E. Endoh, J.K. Leland, A.J. Bard, J. Phys. Chem. 90 (1986) 6223–6226.
[14] N. Zhang, A. Jalil, D.X. Wu, S.M. Chen, Y.F. Liu, C. Gao, W. Ye, Z.M. Qi, H.X. Ju, C.M. Wang, X.J. Wu, L. Song, J.F. Zhu, Y.J. Xiong, J. Am. Chem. Soc. 140 (2018) 9434–9443.
[15] H.Y. Liang, H. Zou, S.Z. Hu, New J. Chem. 41 (2017) 8920–8926.
[16] H.Y. Liang, J.Z. Li, Y.W. Tian, RSC Adv. 7 (2017) 42997–43004.
[17] P.K. Mascharak, G.C. Papaefthymiou, W.H. Armstrong, S. Foner, R.B. Frankel, R.H. Holm, Inorg. Chem. 22 (1983) 2851–2858.
[18] A. Banerjee, B.D. Yuhas, E.A. Margulies, Y.B. Zhang, Y. Shim, M.R. Wasielewski, M.G. Kanatzidis, J. Am. Chem. Soc. 137 (2015) 2030–2034.
[19] K.A. Brown, D.F. Harris, M.B. Wilker, A. Rasmussen, N. Khadka, H. Hamby, S. Keable, G. Dukovic, J.W. Peters, L.C. Seefeldt, P.W. King, Science 352 (2016) 448–450.
[20] L.E. Roth, F.A. Tezcan, J. Am. Chem. Soc. 134 (2012) 8416–8419.
[21] J. Soria, J.C. Conesa, J. Phys. Chem. 95 (1991) 274–282.
[22] O. Rusina, A. Eremenko, G. Frank, H.P. Strunk, H. Kisch, Angew. Chem. Int. Ed. 40 (2001) 3993–3995.
[23] Y.H. Lu, Y. Yang, T.F. Zhang, Z. Ge, H.C. Chang, P.S. Xiao, Y.Y. Xie, L. Hua, Q.Y. Li, H.Y. Li, B. Ma, N.J. Guan, Y.F. Ma, Y.S. Chen, ACS Nano 10 (2016) 10507–10515.
[24] D.V. Yandulov, R.R. Schrock, Science 301 (2003) 76–78.
[25] C. Rebreyend, B. de Bruin, Angew. Chem. Int. Ed. 54 (2015) 42–44.
[26] Y.C. Hao, X.L. Dong, S.R. Zhai, H.C. Ma, X.Y. Wang, X.F. Zhang, Chem. Eur. J. 22 (2016) 18722–18728.
[27] S.S. Song, Z.C. Liang, W.L. Fu, T.Y. Peng, ACS Appl. Mater. Interfaces 9 (2017) 17013–17023.
[28] K. Viswanathan, K. Brandt, E. Salje, J. Solid State Chem. 36 (1981) 45–51.
[29] B. Im, H. Jun, K.H. Lee, J.S. Lee, CrystEngComm 13 (2011) 7212–7215.
[30] P. Biloen, G.T. Pott, J. Catal. 30 (1973) 169–174.
[31] Y. Gorlin, B. Lassalle-Kaiser, J.D. Benck, S. Gul, S.M. Webb, V.K. Yachandra, J. Yano, T.F. Jaramillo, J. Am. Chem. Soc. 135 (2013) 8525–8534.
[32] B.J. Tan, K.J. Klabunde, P.M.A. Sherwood, J. Am. Chem. Soc. 113 (1991) 855–861.
[33] M.A. Stranick, Surf. Sci. Spectr. 6 (1999) 31–38.
[34] Y.H. Chang, Z.G. Wang, Y.-E. Shi, X.C. Ma, L. Ma, Y.Q. Zhang, J.H. Zhan, J. Mater. Chem. A Mater. Energy Sustain. 6 (2018) 10939–10946.
[35] J.J. Wang, L. Tang, G.M. Zeng, Y.C. Deng, Y.N. Liu, L.L. Wang, Y.Y. Zhou, Z. Guo, J.J. Wang, C. Zhang, Appl. Catal. B Environ. 209 (2017) 285–294.
[36] J.J. Wang, L. Tang, G. Zeng, Y.C. Deng, H.R. Dong, Y.N. Liu, L.L. Wang, B. Peng, C. Zhang, F. Chen, Appl. Catal. B Environ. 222 (2018) 115–123.
[37] Y.C. Deng, L. Tang, G.M. Zeng, C.Y. Feng, H.R. Dong, J.J. Wang, H.P. Feng, Y.N. Liu, Y.Y. Zhou, Y. Pang, Environ. Sci. Nano 4 (2017) 1494–1511.
[38] F.P.J.M. Kerkhof, J.A. Moulijn, A. Heeres, J. Electron Spectr. Relat. Phenomena 14 (1978) 453–466.

[39] Z.H. Zhao, Y. Bai, W.W. Ning, J.M. Fan, Z.Y. Gu, H.H. Chang, S. Yin, Appl. Surf. Sci. 471 (2019) 537–544.

[40] R.D. Shannon, Acta Crystallogr. 32 (2015) 751–767.

[41] A.A. Dakhel, J. Supercond. Nov. Magnet. 31 (2017) 2039–2046.

[42] X.X. Zou, G.D. Li, M.Y. Guo, X.H. Li, D.P. Liu, J. Su, J.S. Chen, Chem. Eur. J. 14 (2008) 11123–11131.

[43] C.D. Lv, C.S. Yan, G. Chen, Y. Ding, J.X. Sun, Y.S. Zhou, G.H. Yu, Angew. Chem. Int. Ed. 57 (2018) 6073–6076.

[44] D.N. Hendrickson, J.M. Hollander, W.L. Jolly, Inorg. Chem. 8 (1969) 2642–2647.

[45] K. Li, T.Y. Peng, Z.H. Ying, S.S. Song, J. Zhang, Appl. Catal. B Environ. 180 (2016) 130–138.

[46] P.Z. Wang, M.X. Zhang, W.F. Zhang, C.H. Yang, C.Y. Li, Appl. Catal. A-Gen. 542 (2017) 311–316.

[47] J.X. Lin, L.M. Zhang, Z.Q. Wang, J. Ni, R. Wang, K.M. Wei, J. Mol. Catal. A-Chem. 366 (2013) 375–379.

[48] Z.F. Huang, J.J. Song, X. Wang, L. Pan, K. Li, X.W. Zhang, L. Wang, J.-J. Zou, Nano Energy 40 (2017) 308–316.

[49] S.S. Song, Y.Y. Guo, T.Y. Peng, J. Zhang, R.J. Li, RSC Adv. 6 (2016) 77366–77374.